ADVANCED INTELLIGENT SYSTEMS
Open Access
www.advintellsyst.com

Deep Neural Network Regression-Assisted Pressure Sensor for Decoupling Thermal Variations at Different Operating Temperatures

Joohyung Bang, Keuntae Baek, Jaeyoung Lim, Yongha Han, and Hongyun So**

Decoupling environment-dependent response in sensing techniques is essential for the diverse practical applications. This work presents a novel thermal effect decoupling method for sponge pressure sensors based on a deep neural network (DNN) regression model, which is difficult to achieve owing to the material- and structure-related complex effects of the sponge-based pressure sensor. A poly (3,4-ethylenedioxythiophene):poly(styrenesulfonate)-based multifunctional device is fabricated with a both pressure and thermally responsive part and an only thermally responsive part; and a DNN model with two input features is adapted to implement the substantial pressure prediction system without thermal interference. Proposed model shows the robust decoupled pressure-sensing capability with high accuracy of ≈96.23% using two input features. It also enables accurate pressure prediction under both the thermally steady and transition regions, which indicates significant potential for a precise measurement system. These results demonstrate the possibility of reliable pressure monitoring under varying thermal conditions, which is important for accurately measuring pressure in complex power plants, human–machine interfaces, and compact wearable platforms.

1. Introduction

Despite the rapid development of numerous pressure-sensing technologies, precise pressure-sensing techniques in variable environments are still required for commercial and practical applications.[1,2] Based on material-related properties, various pressure-sensing mechanisms (i.e., piezoresistive,[3,4] capacitive,[5–9] piezoelectric,[10–12] and triboelectric)[13–15] cannot address signal distortion issues under varying conditions, such as temperature[16] and humidity,[17] which makes it difficult to achieve stable sensing. Although the electrical properties of sensing materials under varying conditions have been elucidated,[18] these properties do not match those of the sensors. Specifically, most pressure sensors have complex microstructures, which is the key point of the sensing mechanism;[19] thus, environmental effect-driven electrical distortions become unpredictable owing to material and structure-related complex effects.[20] Therefore, eliminating the environmental effects of sensor signals remains challenging.

Many efforts have been made to address this interference, including structural decoupling,[21,22] calibration,[23–25] and multimode sensing.[26–30] Although these decoupling methods can solve environmental problems, there are still inevitable limitations in practical applications. For instance, the structural decoupling method is accompanied by a complicated fabrication process and complex structure, which makes it difficult to utilize the sensor.[21,22] However, calibration, which is the most commonly used method, has chronic limitations, such as the requirement for additional sensors, complexity in designing circuit boards, and complex relationship formulas.[23–25] Multimode sensing methods have emerged in recent years owing to their simultaneous pressure and temperature detection ability based on separated sensing mechanisms; however, they still have problems with limited decoupling capability, complex signal collecting systems, and the impossibility of steady temperature detection without a thermal gradient.[26–30] Hence, a new method to separate the environmental effects from the originating sensor signal is required for an accurate pressure-monitoring system.

Recently, data-driven deep-learning-based methods have been highlighted as potential new candidates to solve chronic problems that have not yet been solved. Among the various data-driven models, deep neural network (DNN)-based models

J. Bang, K. Baek, H. So
Department of Mechanical Engineering
Hanyang University
Seoul 04763, South Korea
E-mail: hyso@hanyang.ac.kr

J. Lim, Y. Han
Automotive, Research & Development Division
Hyundai Motor Group
Hwaseong 18280, South Korea
E-mail: jytree@hyundai.com

H. So
Institute of Nano Science and Technology
Hanyang University
Seoul 04763, South Korea

The ORCID identification number(s) for the author(s) of this article can be found under https://doi.org/10.1002/aisy.202300186.

DOI: 10.1002/aisy.202300186

have the advantage of demonstrating complex nonlinear relationships between the input and output parameters. Thus, DNN-based methods have been widely used to reveal relationships in various applications, such as multipoint contact estimation,[31] cough prediction,[32] thermal mapping,[33] cancer screening,[34] nanocomposite property prediction,[35] inverse design,[36] and wearable electronics.[37] However, the thermal effect decoupling of the sensor signal distorted by the material and structure-related complex effects has not been reported.

Herein, we propose a facile fabrication method for a poly (3,4-ethylenedioxythiophene):poly(styrenesulfonate) (PEDOT:PSS)-coated sponge-type pressure sensor integrated with PEDOT:PSS-coated paper as the thermally responsive layer, and a thermal effect decoupling method for the proposed pressure sensor using a DNN-based regression model. The fabricated sponge and paper demonstrated reliable sensing capabilities in terms of pressure and temperature, respectively; however, the sponge showed temperature-dependent responses owing to its material and structure-related nonlinear properties. To separate the environmental effects from the original sensor signal, the currents of both the sponge and paper were selected as the input features, and the applied pressure was set as the output feature. Using the proposed DNN-based thermal decoupling model with two input features, the sponge sensor exhibited temperature-dependent responses, demonstrating substantial pressure prediction performance without thermal interference. Notably, the proposed DNN model also demonstrated effective pressure prediction performance under both the thermal transition and steady regions, which was difficult to achieve using other decoupling methods, demonstrating its potential for a precise measurement system. These results support a reliable pressure monitoring system in diverse thermal environments, which is important for accurate pressure measurements, such as in complex power plants, human–robot interfaces, and wearable platforms.

2. Results and Discussion

2.1. Sensor Design and Preparation

The main concept of the decoupling system is illustrated in **Figure 1**. The proposed sensor has two main sensing parts: a pressure and thermally responsive sponge and thermally responsive paper. The two parts were integrated into a single polyethylene terephthalate (PET) film to be affected by identical temperature conditions. Although the sponge is sensitive to pressure under varying thermal conditions, it shows an unexpected current level that depends on the pressure intensity. To address this problem, a DNN regression-based thermal decoupling system for a pressure sensor was introduced using two signals (i.e., sponge and paper signals) as input features.

The overall sensor preparation process is illustrated in **Figure 2**a. Commercially available melamine sponge and paper with double-sided tape attached were cut into customized sizes. Because both melamine sponges and paper have superhydrophilic properties and microstructures, they are appropriate for dip-coating with PEDOT:PSS aqueous solutions. Therefore, both the sponge and the paper were immersed in the PEDOT:PSS solution for full absorption. Then, both the sponge and paper were dried at a high temperature until all water was fully evaporated. PEDOT:PSS and melamine are all polymers with aromatic heterocyclic groups; thus, PEDOT:PSS can be well coated on the surface of melamine sponge due to π–π stacking, which may enhance the intermolecular interactions between two materials.[29,30,38] Paper is mostly made up of cellulose, so PEDOT:PSS and paper can be easily compounded through hydrogen-bonding interactions.[39] Optical and scanning electron microscopy (SEM) images of the PEDOT:PSS-coated sponge and paper are shown in Figure 2b,c. The sponge had polymeric skeleton structures with high porosity (Figure 2b), which enhanced the compressibility with applied pressure. Tangled cellulose structures, which increase surface area, were also observed in the paper. After drying, the PEDOT:PSS-coated paper was attached to the PET film as a temperature-sensing part by removing the protective film of the preattached double-sided tape; further, the PEDOT:PSS-coated sponge and conductive nylon fabric tapes were attached to the same PET film as the pressure-sensing part and electrodes, respectively. It should be noted that two sensing parts (i.e., sponge and paper) were attached at a distance of 3 mm to avoid the direct pressure effects on the paper. Finally, an additional PET film was attached to the top surface of the sponge using double-sided tape as a protective layer. An optical image of the assembled device is shown in Figure 2d.

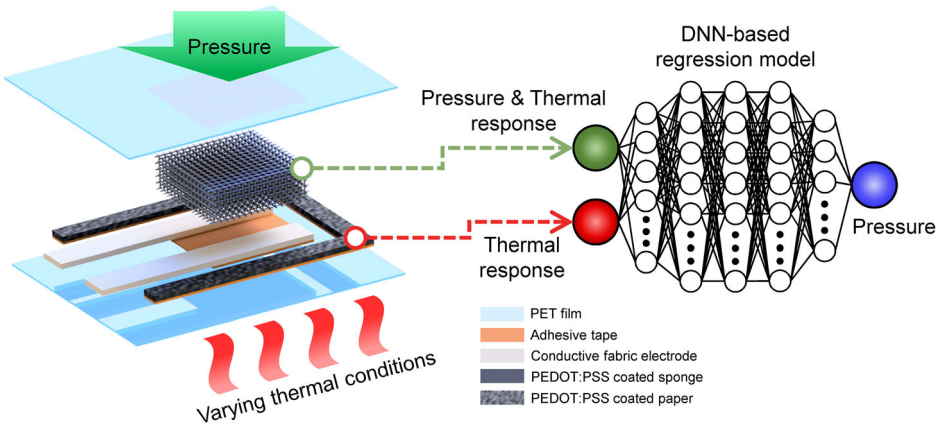

Figure 1. Schematics and concept image of the DNN-based thermal effects decoupling system.

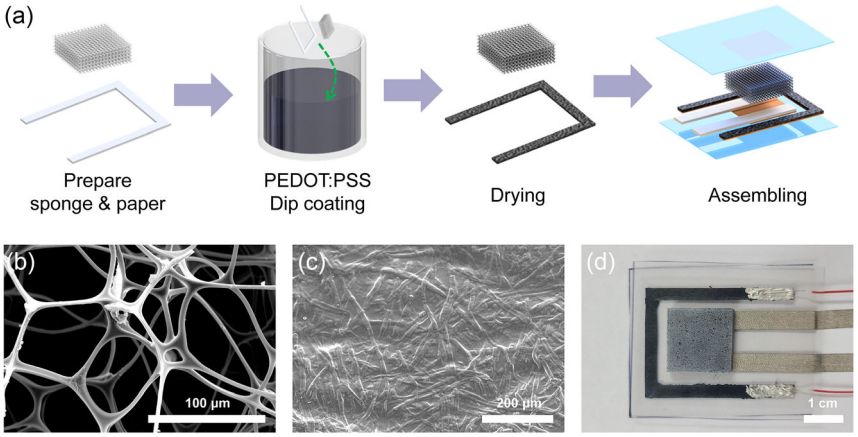

Figure 2. Schematics and images of the fabricated PEDOT:PSS-based device. a) Schematic of the fabrication process of the proposed multifunctional device. b) SEM image of the PEDOT:PSS-coated melamine sponge. c) SEM image of the PEDOT:PSS-coated paper. d) Optical image of the proposed multifunctional device.

2.2. Characterization and Measurements

Various experiments were conducted to characterize the pressure- and temperature-sensing capabilities of the fabricated sponges and paper, respectively. To stabilize the signal, all experiments were conducted after several decades of compression and heating/cooling cycles on sponge and paper, respectively. Pressure sensitivity (S_p) was defined as $S_p = (\Delta I_{sponge}/I_{0,sponge})/P$, where ΔI_{sponge} represents the current change in the sponge, $I_{0,\ sponge}$ represents the current in the sponge without pressure, and P represents the pressure applied to the sponge. P was calculated as $P = F/A$, where F represents the applied force and A represents the horizontal area of the sponge, which was unified as 1.7 cm $\times$ 1.7 cm in this study. The temperature sensitivity (S_t) was defined as $S_t = (\Delta I_{paper}/I_{0,paper})/\Delta T$, where ΔI_{paper} represents the current change of the paper, $I_{0,paper}$ represents the current through paper at a room temperature of 25 °C, and ΔT represents the temperature change in comparison with the room temperature of 25 °C.

The pressure-sensing mechanism of the sponge is shown in **Figure 3**a. The PEDOT:PSS was well coated on internally connected porous microstructures based on π–π stacking;[29,30,38] therefore, all the polymeric skeleton structures have good electrical conductivity through coated PEDOT:PSS. The coated sponge also has excellent elasticity based on its material and structural properties; therefore, the microstructures of the sponge can easily deform with the applied compressive force. Therefore, the skeleton microstructure makes more contact because of the applied pressure, which lowers the resistance and enhances the current signal with the enhanced current pathways based on the piezoresistive mechanism. As shown in Figure 3b, to characterize the performance of the sponge, a sensitivity test was conducted using a tensile tester and a 3D-printed stamp with an identical sponge size. When pressure was applied to the sponge for 5 s, the sensitivity point was measured by matching the highest current signal with the highest force. The sensing range of the sensor can be divided into three linear regions: 0–50 kPa at 0.595 kPa^{-1}, 50–500 kPa with 1.56 kPa^{-1}, and 500–865 kPa at 1.03 kPa^{-1}. Note that with increasing pressure intensity, the sensitivity increases near 50 kPa region. This tendency may be elucidated with enhanced contact between sponge and fabric electrodes. Conversely, at high pressure region near 500 kPa, the sensitivity deterioration has observed, and this can be resulted from the porous conducting network densification.[30] The dynamic sensing responses at various pressures are shown in Figure 3c. Our sponge demonstrated a stable and repeatable pressure-sensing performance without noticeable current drift over a wide pressure range. Figure 3d depicts the current–voltage (I–V) curves from −1 to 1 V under different applied pressures. The I–V curves show a good linear signal, which represents good Ohmic contact and a stable sensor signal obtained through the sponge. The sensor also exhibited good response/recovery times of 194/206 ms at a minimum detectable resolution of 1695.5 Pa (Figure 3e). To verify the long-term durability of the sponge, a cycle test was conducted under a high pressure of 220 kPa for 2000 times (Figure 3f). The sponge exhibited a stable pressure-sensing performance without significant deterioration, indicating that it is a reliable monitoring platform for pressure data acquisition.

The temperature-sensing mechanism used in this study is illustrated in **Figure 4**a. The PEDOT:PSS has a temperature-dependent conductivity under typical temperatures between 0 and 75 °C, based on the interlayer swelling and water absorption/desorption behavior of PEDOT:PSS grains.[18] The PEDOT:PSS nanostructure generally forms core–shell structure grains based on PEDOT-rich cores and PSS-rich shells. The insulating PSS boundaries contributed significantly to the overall conductivity and swelled with the absorbed water molecules at room temperature, which decreased the conductivity. When the paper was heated, the absorbed water molecules began to desorb; thus, higher conductivity was achieved through PSS boundary size reduction. Based on these mechanisms, PEDOT:PSS can be used to detect temperature changes effectively. In addition, because PEDOT:PSS is commercially

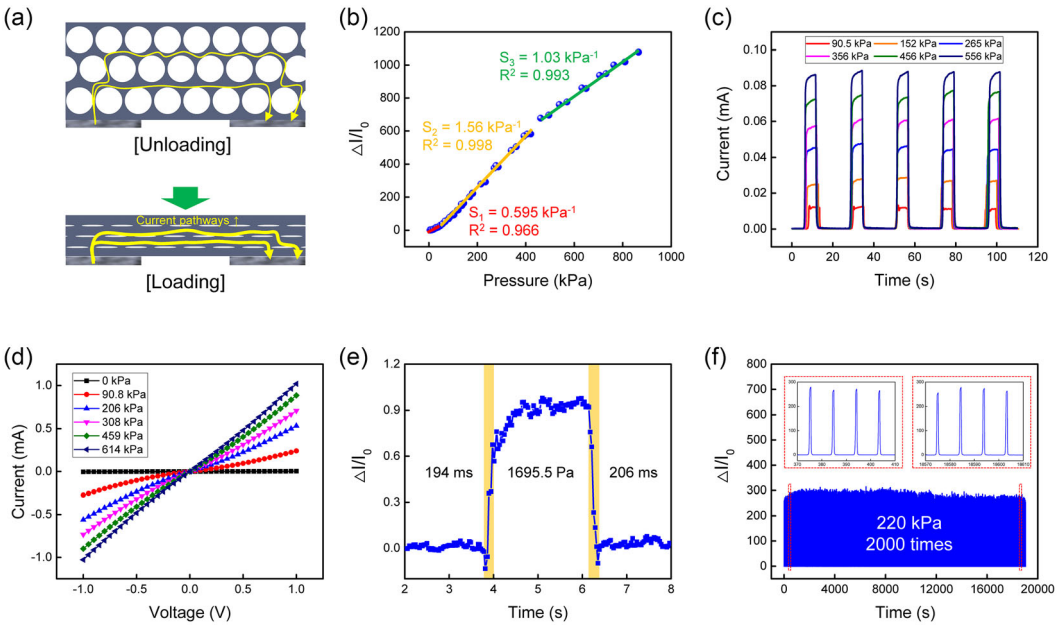

Figure 3. Pressure-sensing mechanism and sensing performance of the PEDOT:PSS-coated sponge. a) Schematic of the pressure-sensing mechanism of the sponge. b) Relative current responses of the sponge under different pressures (0–865 kPa). c) Dynamic responses of the sponge. d) Current–voltage curves of the sponge with different pressures (0–614 kPa) as voltage sweeping from −1 to 1 V. e) Response and recovery time of the sponge under a 1695.5 Pa pressure. f) Durability test results of the sponge after 2000 loading/unloading cycles under a pressure of 220 kPa.

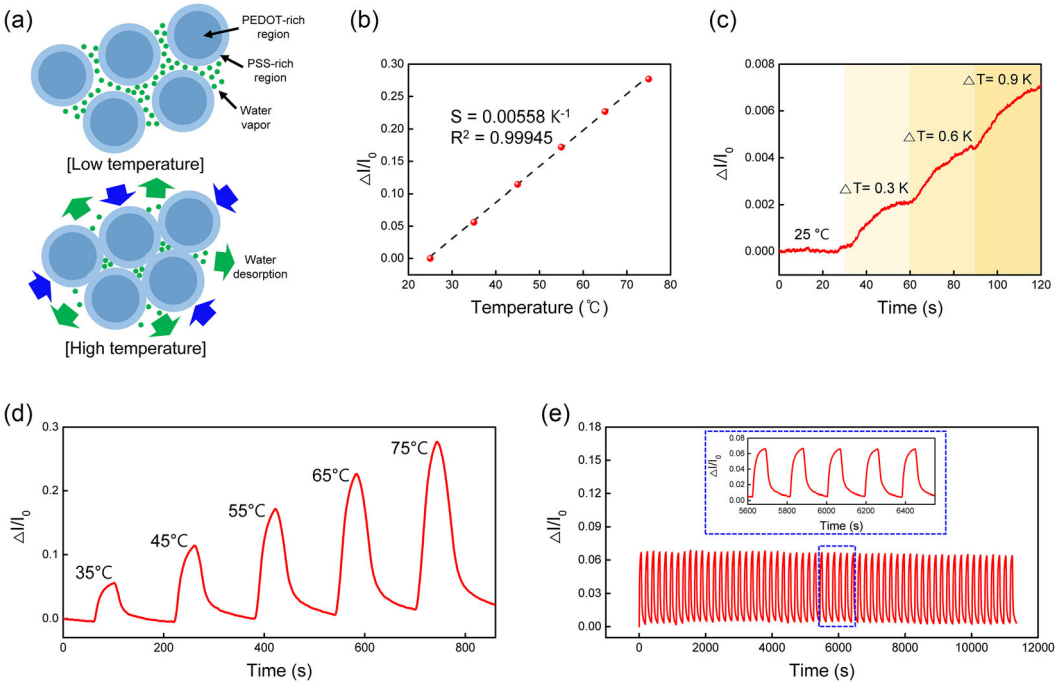

Figure 4. Temperature-sensing mechanism and sensing performance of the PEDOT:PSS-coated paper. a) Schematic of the temperature-sensing mechanism of the paper. b) Relative current responses of the paper under different temperatures (25–75 °C). c) Minimum temperature-sensing resolution test of the paper. d) Dynamic responses of the paper. e) Durability test results of the paper after 60 heating/cooling cycles.

used as an aqueous solution, paper can be coated well with PEDOT:PSS owing to its superhydrophilicity and good interconnections (i.e., hydrogen bonding). Furthermore, PEDOT:PSS-coated paper has a large surface area owing to the cellulose structure; therefore, the aforementioned mechanisms can be enhanced well.

To characterize the temperature-sensing performance of the paper, a temperature-controlled chamber was used in various experiments. Figure 4b shows the relative current sensitivity of the paper at intervals of 10 °C, from 25 to 75 °C. The sensitivity point was measured by matching the highest current signal and temperature when the paper was heated in the chamber for 60 s. The paper shows great temperature-sensing capability in wide range with the sensitivity of $0.00558\,K^{-1}$ with high linearity (coefficient of determination, $R^2 = 0.99958$). A minimum temperature-sensing resolution test was conducted, as shown in Figure 4c. The paper exhibited its potentiality to detect the temperature change of at least 0.3 °C without noticeable current signal fluctuation. The dynamic sensing responses at various temperatures are presented in Figure 4d. The paper was heated for 60 s and cooled to the room temperature of 25 °C for 120 s, demonstrating its stable, linear, and accurate temperature-sensing performance. In addition, to verify the durability and repeatability of the paper, a temperature cycle test was conducted under heating to 35 °C for 60 s and cooling to 25 °C for 120 s, for 60 times. The paper demonstrated its reliable temperature-sensing performance without significant deterioration and current drift, which indicates a trustworthy monitoring platform for temperature data acquisition.

In addition, a comparison of the sensing performance between the sensor developed in this study and previously reported multifunctional sensors was conducted and listed in **Table 1**. The sensor developed in this study has demonstrated its notable characteristics with broad pressure-sensing range and temperature sensing with high pressure.

2.3. Dataset Acquisition

To collect the dataset with varying temperature–pressure environments, a testbed was prepared using a digital hot plate and tensile testing machine, as shown in **Figure 5**. Based on these two instruments, the testbed could implement and control both the temperature and pressure conditions simultaneously. The step increasing pressures with 14 steps were applied to measure and collect the current data, depending on varying temperature conditions (24.6, 33.7, 43.0, 52.4, 61.6, and 70.6 °C). In particular, the maximum force that the digital hot plate could withstand was 80 N; therefore, the pressure range was fixed from 0 to 80 N. Based on the aforementioned thermal effects of PEDOT:PSS, both the sponge and paper showed positive temperature coefficients for the current signal (**Figure 6**a–c). Figure 6a shows the current signals collected from the sponge using the prepared testbed. Owing to the atypical responses caused by the changing conductivity with varying temperature, the sponge did not maintain its current level, although an identical pressure was applied. To utilize the acquired data to train the deep-learning regression model, the collected dataset was composed of two input parameters (sponge current and paper current) and an output parameter (applied pressure). Figure 6b,c shows the current

Table 1. Comparison of the present sensor with other multifunctional pressure–temperature sensors.

Materials	Pressure-sensing mechanism	Pressure sensitivity [kPa^{-1}]	Pressure-sensing range [kPa]	Temperature-sensing mechanism	Temperature-sensing limit [K]	Temperature-sensing with high pressure	References
PDMS/graphene	Resistive	0.51–15.22	0–45	Thermoelectric	1	X	[26]
Polyurethane/PEDOT:PSS	Resistive	4.3–28.9	0–20	Thermoelectric	0.1	X	[27]
TPU/CNFs	Resistive	0.14–0.51	0–120	Thermoelectric	0.05	O	[28]
Melamine/PEDOT:PSS/CNT	Resistive	0.04–1.97%	0–100	Thermoelectric	0.05	X	[29]
Melamine/PEDOT:PSS/CNT	Resistive	0.18–3.35%	0–100	Thermoelectric	0.4	X	[30]
Melamine/PEDOT:PSS	Resistive	0.595–1.56	0–865	Resistive	0.3	O	This work

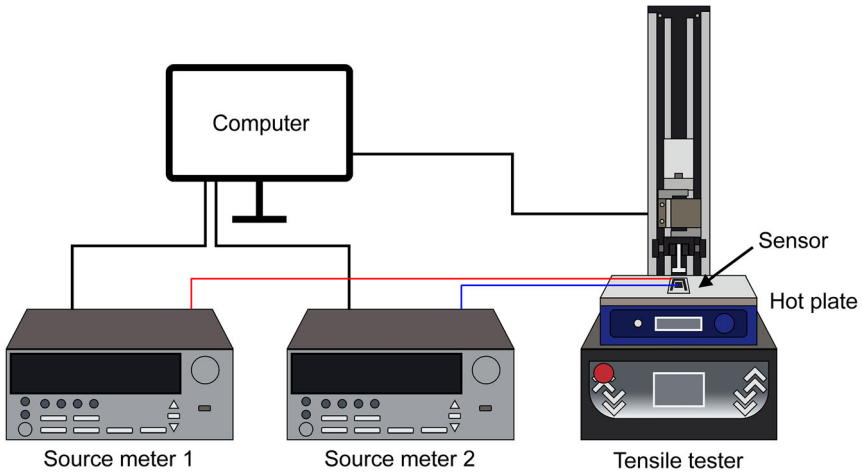

Figure 5. Schematic of the experimental setup for data acquisition with varying temperature–pressure environment.

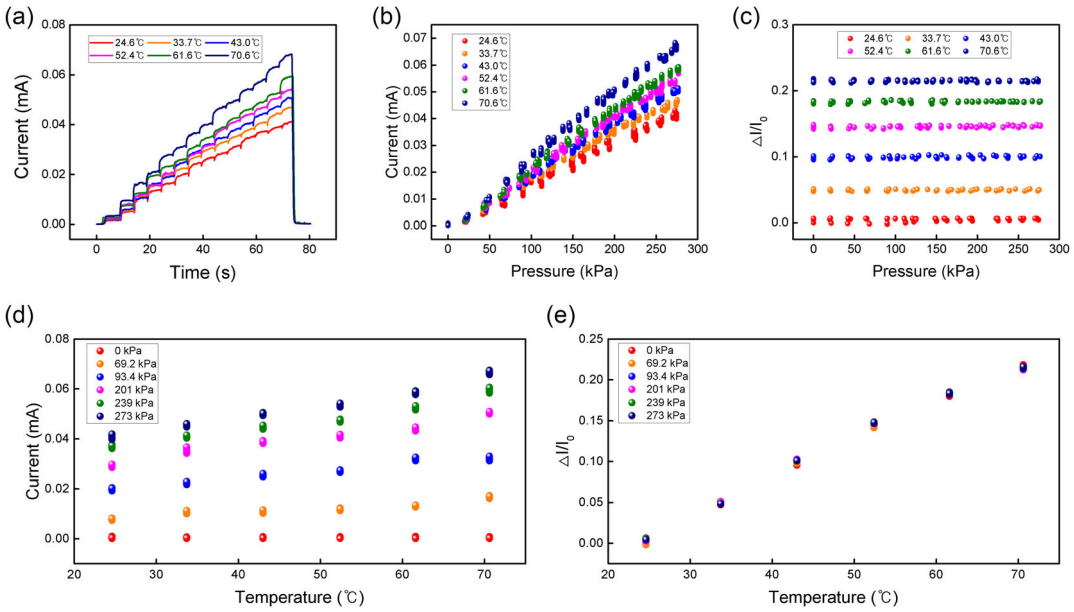

Figure 6. Training dataset acquisition test results of the proposed multifunctional device. a) Time-dependent responses of the sponge under different temperature. Sample of input and output features utilized for decoupling system; current through b) sponge and c) paper under pressure and thermal variations. Temperature-dependent current variation through d) sponge and e) paper under different pressure.

response of the sponge and the relative current response of the paper, respectively, as the input parameters of the collected dataset. To obtain the reliable training dataset, the current data of the sponge were restrictively extracted when the drastically changing signal with applied pressure starts converging (i.e., 0.3 s after the pressure was applied). In addition, all training datasets were collected when the relative current signal of the paper was fully converged (i.e., 200 s after the hot plate). Because the proposed pressure sensor has a complex 3D structure, the thermal effects on the current signals became unpredictable under varying thermal and applied pressure conditions. Owing to unpredictable temperature effects, pressure sensors with complex 3D structures cannot accurately measure the pressure with varying current levels. Figure 6d,e shows the temperature-induced current variation of the sponge and the paper under different pressures, respectively. Due to the temperature-dependent conductivity of PEDOT:PSS, both signals exhibit the positive correlation between the current and temperature.

2.4. Dataset Preparation and DNN Model

In this study, we utilized Python-based open-source libraries (e.g., TensorFlow and Keras) to prepare the dataset (i.e., training, validation, and test datasets) and train the deep learning regression model. For dataset preparation, 8016 different data points with 230 different input and output features were obtained. The prepared dataset was divided into two parts (training and validation datasets) for training and average performance evaluation of the proposed model. Thus, the prepared dataset was randomly split at a ratio of 8:2 into the training and validation datasets. Notably, the test dataset did not overlap with the prepared dataset because it was prepared separately from the training and validation datasets and was randomly obtained with 2281 different data points for 58 different cases. Prior to training the deep learning regression model, the input features were preprocessed to improve the convergence speed using the following min–max scaling method[40]

$$X_{\text{scaled}} = \frac{x - x_{\min}}{x_{\max} - x_{\min}} \tag{1}$$

where X_{scaled}, $x_{\min}$, and $x_{\max}$ denote the scaled, minimum, and maximum values of x, respectively.

The proposed DNN regression model architecture for the thermal effect decoupling method is shown in **Figure 7**a. As observed in the proposed model architecture, the current through the sponge and the normalized current through the paper were used as input parameters, and the applied pressure was utilized as an output parameter. Furthermore, hidden layers, including four fully connected layers and a dropout layer, were used as regression layers. The four fully connected layers have 16, 256, 128, and 64 nodes. In addition, a rectified linear unit (ReLU), which has the benefits of low computational time and nonlinear properties for regression models, was used for every fully connected layer as the activation function.[41] In terms of deep learning model training, overfitting, which increases errors through overlearning of the training dataset, is emerging as a severe issue.[42,43] To date, several methods (i.e., such as dropout,[44,45] batch normalization,[46,47] and early stopping[48,49]) have been introduced to address the overfitting issue in regression model training. The dropout method was used to prevent the overfitting problem in this study. Detailed information on the model training is listed in **Table 2**.

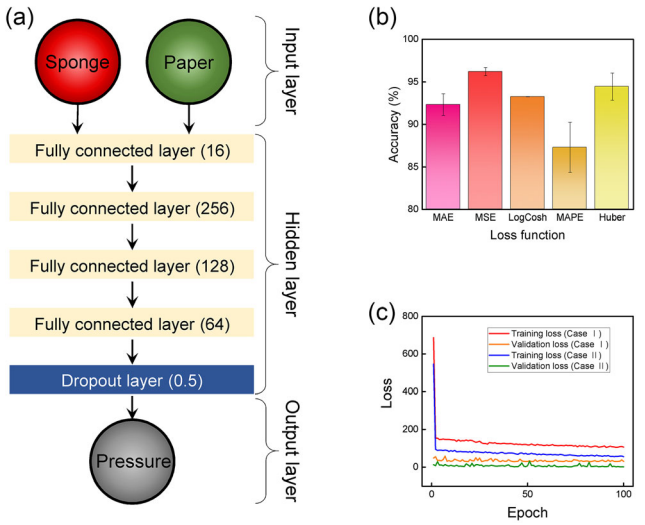

Figure 7. Design of the DNN model-based decoupling system. a) Illustration of DNN regression architecture for decoupling system. b) Comparison of prediction accuracy using MAE, MSE, LogCosh, MAPE, and Huber as loss functions. c) Training and validation loss trends depending on the epochs using the different input features of only sponge signals (case I), and sponge and paper signals (case II).

Moreover, the mean absolute percentage error (MAPE) was employed for model scores to evaluate the model performance based on the proposed loss functions. The MAPE is defined as follows

$$\mathrm{MAPE} = \frac{1}{n}\sum_{i=1}^{n}\left|\frac{T_i - P_i}{T_i}\right| \times 100\% \quad (2)$$

where T_i, P_i, and n are the true value, predicted value, and the number of data points, respectively. Because the MAPE represents the percentage error, the model prediction accuracy can also be defined (model accuracy (%) = 100–MAPE) for the overall model performance evaluation.

2.5. Demonstration of Prediction Performance

To find an effective loss function for the proposed model, various loss functions, such as the mean absolute error (MAE), mean squared error (MSE), log hyperbolic cosine (LogCosh), MAPE, and Huber, were utilized. Each model was trained 3 times with the newly shuffled training and validation datasets and compared with the overall model prediction performance. As a result, the model with MSE loss function exhibited the highest prediction accuracy of ≈96.23% compared to prediction models with other loss functions (i.e., MAE, LogCosh, MAPE, and Huber), as shown in Figure 7b. Note that the average accuracy of the prediction model with MSE loss function was ≈8.92% higher than the trained model with MAPE loss function, which exhibited the lowest prediction performance. Therefore, the MSE loss function was adopted to train the subsequent deep learning regression model for the different cases. The scores of the proposed model with five different loss functions are listed in **Table 3**.

To demonstrate the demand for a thermally responsive layer for the proposed decoupling system, two cases (cases I and II) were introduced and compared. Specifically, the trained model using only the sponge current as the input layer is defined as case I, whereas the trained model using both the sponge current and normalized paper current as the input layer is defined as case II. Figure 7c shows the overall convergence trends of the training and validation losses for the trained model for the two cases (cases I and II). Although the training and validation losses of the two cases exhibited sufficient convergence, both the training and validation losses of case II were lower than those of case I. Specifically, the validation loss of case I exhibited a ≈19.7 times higher value than that of case II, which indicates the overall error of the trained model. These results reveal that the proposed model for case II is more suitable for thermal decoupling systems than the prediction model for case I.

To evaluate the performance of the DNN regression model, the predicted results of the trained model for two cases (cases I and II) and the true values derived from the prepared test dataset were compared, as shown in **Figure 8**a,b, respectively. In this plot, the black dots and red lines indicate the predicted results of the trained model and the true values obtained from the experiment for the test dataset, respectively. Therefore, as more black dots cluster near the red line, the proposed regression model exhibits a better prediction performance. For this reason, a trained model with case II, where black dots were closely clustered to the red line, demonstrated the high performance compared to a trained model with case I. Quantitatively, a trained model with cases I and II showed an average accuracy of ≈88.38% and ≈96.23%, respectively. Thus, case II demonstrated ≈7.85% higher prediction performance compared to the case I, as depicted in Figure 8c.

To evaluate the prediction performance of the model trained in cases (cases I and II) under varying thermal and pressure conditions, an additional time-dependent test dataset was prepared. Figure 8d–f represents the input data of the additional time-dependent test dataset, the predicted result of the model trained in case I, and the predicted result of the model trained in case II, respectively. As depicted in Figure 8d, the plot is composed of a red line (i.e., the normalized current of paper) and a blue line (i.e., the current of the sponge). Specifically, the normalized current of the paper (red line) only varies with thermal variation, whereas the current of the sponge (blue line) varies under

Table 2. DNN parameters for model training.

Parameter	Value
Activation function	ReLU
Optimizer	Adam
Epoch	100
Dropout rate	0.5

Table 3. Evaluated average accuracy of the trained model depending on the different loss functions.

Loss function	MAE	MSE	LogCosh	MAPE	Huber
Accuracy	92.3238%	96.2255%	93.2602%	87.3029%	94.4490%

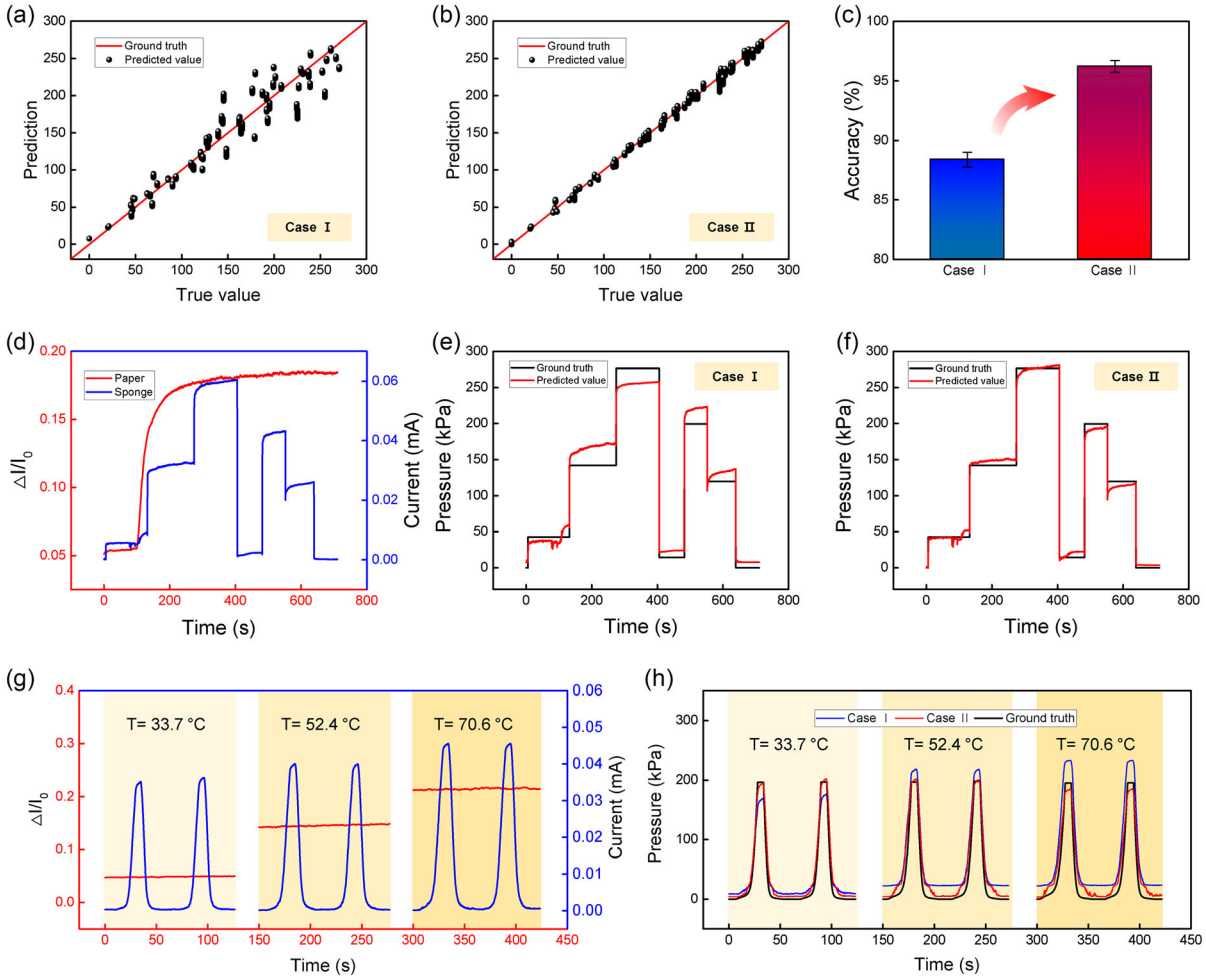

Figure 8. Performance of the proposed DNN regression-based thermal effects decoupling system. a,b) The cross-plot between the true and predicted values of the model trained with (a) case I and (b) case II. c) Accuracy comparison of the trained model with case I and case II. d) Original signals of the first test dataset. e,f) Prediction results of the first test dataset using the trained model of (e) case I and (f) case II. g) Original signals of the second test dataset. h) Prediction results of the second test dataset using the trained model of case I and case II.

both thermal and pressure variations. The temperature was changed from 33.7 to 61.6 °C when the time exceeded 100 s. The temperature of hot plate has been increased to reach the specified temperature for ≈90 s. Moreover, the applied pressure was changed arbitrarily with seven steps (i.e., 0, 42.73, 119.95, 142.27, 199.55, and 276.37 kPa). Note that the current of the sponge (i.e., blue line) increases without applied pressure between 100 and 130 s because the current of the sponge is affected by thermal effects. In Figure 8e,f, the plot is composed of a black line (i.e., the true value of the applied pressure) and a red line (i.e., the predicted value of the proposed model). As depicted in Figure 8e, the prediction model with case I showed low reliability because the red line (i.e., the predicted value of the proposed model) and black line (i.e., the true value of the applied pressure) did not match. However, the proposed model with case II shows a high prediction performance, as indicated by the red line (i.e., the predicted value of the proposed model) and black line (i.e., the true value of the applied pressure), almost matching, as depicted in Figure 8f. It should be noted that in the time step between 100 and 130 s, the proposed model with case II exhibited a predicted value that was close to the true value, whereas the model with case I showed an abnormal signal. In addition, it should be noted that, unlike the trained model with case I, the proposed model with case II can almost accurately predict the applied pressure under varying thermal conditions (i.e., a time step between 100 and 250 s). These results reveal that the DNN regression model for case II has the potential to be applied to reliable monitoring systems under varying thermal and pressure conditions. Furthermore, dynamic pressure response test was conducted to demonstrate the potential of proposed decoupling method. Figure 8g,h represents the input data and the predicted pressure results of cases (cases I and II) under the dynamic pressure response, respectively. The test was conducted under identically applied pressure and three different temperature conditions of 33.7, 52.4, and 70.6 °C, respectively. As shown in Figure 8g, the input data of dynamic pressure test are composed of a red line (i.e., the normalized current of paper) and a blue line (i.e., the current of the sponge). When the

identical pressure was applied, the sponge signal (i.e., the blue line in Figure 8g) exhibits the upregulating trend with increasing temperature. The predicted results of cases I, II, and ground truth of the applied pressure are indicated as blue, red, and black lines in Figure 8h, respectively. As the temperature increases, the predicted results of case I show the upregulating trend as similar with the input signal of sponge (i.e., the blue line in Figure 8g). As the result, the blue line did not match with the black line in different temperature conditions. Meanwhile, the red line almost matched with the black line, even though the sponge signal was coupled with varying temperature. Thus, the temperature influence of pressure sensor could be ruled out using the propose model with case II.

3. Conclusion

We developed a thermal effect-decoupling system for a PEDOT:PSS-based sponge pressure sensor using a DNN regression model. The proposed DNN regression model successfully addressed temperature-dependent nonlinear signal distortion issues, which originated from material and structural effects, with a simply fabricated PEDOT:PSS-based multifunctional device. To demonstrate the decoupling performance of our DNN regression model-based sensor system, experiments were conducted under various thermal and pressure conditions. Consequently, the proposed DNN model with MSE loss function showed the robust decoupled pressure-sensing capability with high accuracy of ≈96.23%, which is difficult to achieve using a single pressure sensor signal. It also enabled almost accurate pressure prediction under both thermally steady and transition regions, which indicates its significant potential as a precise measurement system. Namely, the proposed model can realize the pressure classification and not be affected by temperature variation. In addition, owing to the strong merits of nonlinear prediction with a DNN-based regression model, additional environments (i.e., varying humidity and magnetic fields) can be considered in future studies. Furthermore, the proposed system can be widely applied for various types of pressure sensors by adjusting the input function using transfer learning. Based on these results, the proposed model can be a promising method for reliable pressure monitoring systems in diverse thermal environments that require accurate pressure measurements, such as complex power plants, human–machine interfaces, and compact wearable platforms.

4. Experimental Section

Fabrication of the Sensor: The commercially available melamine sponge (Magic Sponge, BASF) was first cut into the $1.7 \times 1.7 \times 3$ cm, and the paper (A4, Double A) with attached double-sided tape was cut into a properly predesigned pattern with 3 mm width. Then, the melamine sponge and paper were immersed into the pure PEDOT:PSS (739332-100G, 1.1% in H_2O; Sigma–Aldrich) for 15 min. After immersion, the melamine sponge and paper were carefully squeezed and dried at 170 °C for 2 h to fully evaporate the water. The dried paper was attached to a precut PET (4×5 cm) and connected to copper wires with a conductive silver paste at 70 °C for 30 min. To implement the simultaneous measurement of both pressure and temperature in an integrated single device, conductive nylon fabric tape (5 mm wide, Adafruit Industries) and a dried sponge were attached to the same PET film with double-sided tape. Finally, a PET film was attached to the top layer of the sponge using a double-sided tape as a protective layer.

Characterization of the Sensor: The electrical performances of the sponge and paper were measured using digital source meters (SMU 2611 B and SMU 2614 B, Keithley Instruments Ltd.), respectively. The applied voltage was 0.1 V during the measurements. A temperature-controlled chamber (THMS600PS, Linkam Scientific Instruments Ltd.) was used to characterize the temperature-sensing capability of the paper. A tensile testing machine (MCT-2150, A&D Co.) was used to apply compressible strain to the sponge. The microstructures of the coated sponge and paper were observed using SEM (Quattro ESEM, Thermo Scientific).

Data Acquisition Setting: A digital hot plate (HP-20D, DAIHAN Scientific) and the same tensile testing machine were simultaneously used to implement varying pressure and temperature conditions, as shown in Figure 5. The temperature of hot plate was set from 25 to 75 °C at intervals of 10 °C, and detailed temperatures were measured with a thermocouple. The applied force was measured using the load cell data of the tensile testing machine, and the force data were calibrated as the peak value was sustained while the tensile tester was stopped and no more movements were observed.

Acknowledgements

J.B. and K.B. contributed equally to this work. This work was supported by a Hyundai NGV grant funded by the Hyundai Motor Company and the Korea Institute of Energy Technology Evaluation and Planning (KETEP) and Ministry of Trade, Industry, and Energy (MOTIE) of the Republic of Korea (grant no. 20212020800090).

Conflict of Interest

The authors declare no conflict of interest.

Data Availability Statement

The data that support the findings of this study are available from the corresponding author upon reasonable request.

Keywords

decoupling, deep neural networks, poly(3,4-ethylenedioxythiophene): poly(styrenesulfonate) (PEDOT:PSS), pressure sensors, thermal effects

Received: April 14, 2023
Revised: July 8, 2023
Published online: August 17, 2023

[1] H. Zhang, S. Ju, X. Jin, Y. Yuan, Y. Wu, A. K. Nadda, A. Pugazhendhi, L. Cai, C. Xia, *Renewable Sustainable Energy Rev.* **2022**, *169*, 112915.
[2] S. Wang, F. Gao, Y. Hu, S. Zhang, H. Shang, C. Ge, B. Tan, X. Zhang, J. Zhang, P. Hu, *Chem. Eng. J.* **2022**, *443*, 136446.
[3] Y. Jung, J. Choi, W. Lee, J. S. Ko, I. Park, H. Cho, *Adv. Funct. Mater.* **2022**, *32*, 2201147.
[4] B. Chen, L. Zhang, H. Li, X. Lai, X. Zeng, *J. Colloid Interface Sci.* **2022**, *617*, 478.
[5] C. Lv, C. Tian, J. Jiang, Y. Dang, Y. Liu, X. Duan, Q. Li, X. Chen, M. Xie, *Adv. Sci.* **2023**, *2206807*, 2206807.
[6] Y. Zhong, F. Gu, L. Wu, J. Wang, S. Dai, H. Zhu, G. Cheng, J. Ding, *J. Alloys Compd.* **2023**, *934*, 167919.

[7] M. Zhang, M. Gu, L. Shao, G. Cheng, H. Gao, B. Sun, S. Li, T. Tang, N. Li, Y. Yi, D. Wei, C. Yang, D. Wei, *ACS Appl. Mater. Interfaces* **2023**, *15*, 15884.
[8] R. Qin, M. Hu, X. Li, T. Liang, H. Tan, J. Liu, G. Shan, *Microsyst. Nanoeng.* **2021**, *7*, 100.
[9] R. Qin, G. Shan, M. Hu, W. Huang, *Mater. Today Phys.* **2021**, *21*, 100527.
[10] X. Liu, J. Tong, J. Wang, S. Lu, D. Yang, H. Li, C. Liu, Y. Song, *J. Mater. Chem. C* **2023**, *11*, 4614.
[11] D. Bin Kim, J. Han, S. M. Sung, M. S. Kim, B. K. Choi, S. J. Park, H. R. Hong, H. J. Choi, B. K. Kim, C. H. Park, J. H. Paik, J.-S. Lee, Y. S. Cho, *npj Flexible Electron.* **2022**, *6*, 69.
[12] J. Li, G. Zhou, Y. Hong, W. He, S. Wang, Y. Chen, C. Wang, Y. Tang, Y. Sun, Y. Zhu, *Sens. Actuators, A* **2022**, *337*, 113415.
[13] J. Syamini, A. Chandran, *ACS Appl. Electron. Mater.* **2023**, *5*, 1002.
[14] Y. Zhong, J. Wang, L. Han, S. Dai, H. Zhu, J. Hua, G. Cheng, J. Ding, *Sens. Actuators, A* **2023**, *349*, 114013.
[15] D. Lu, T. Liu, X. Meng, B. Luo, J. Yuan, Y. Liu, S. Zhang, C. Cai, C. Gao, J. Wang, S. Wang, S. Nie, *Adv. Mater.* **2023**, *35*, 2209117.
[16] Y. Hou, L. Wang, R. Sun, Y. Zhang, M. Gu, Y. Zhu, Y. Tong, X. Liu, Z. Wang, J. Xia, Y. Hu, L. Wei, C. Yang, M. Chen, *ACS Nano* **2022**, *16*, 8358.
[17] Y. Liu, Z. Sheng, J. Huang, W. Liu, H. Ding, J. Peng, B. Zhong, Y. Sun, X. Ouyang, H. Cheng, X. Wang, *Chem. Eng. J.* **2022**, *432*, 134370.
[18] J. Zhou, D. H. Anjum, L. Chen, X. Xu, I. A. Ventura, L. Jiang, G. Lubineau, *J. Mater. Chem. C* **2014**, *2*, 9903.
[19] Z. Shi, L. Meng, X. Shi, H. Li, J. Zhang, Q. Sun, X. Liu, J. Chen, S. Liu, *Nano-Micro Lett.* **2022**, *14*, 141.
[20] Z.-X. Li, X.-Y. Gao, P. Huang, Y.-Q. Li, S.-Y. Fu, *J. Mater. Chem. A* **2022**, *10*, 9114.
[21] Y. Chen, H. Lei, Z. Gao, J. Liu, F. Zhang, Z. Wen, X. Sun, *Nano Energy* **2022**, *98*, 107273.
[22] B. Sun, J. Xiong, Z. Fang, L. Gao, A. Xu, P. Jia, Q. Feng, C. Li, *IEEE Sens. J.* **2023**, *23*, 7570.
[23] M. Aryafar, M. Hamedi, M. M. Ganjeh, *Measurement* **2015**, *63*, 25.
[24] S. Cho, H. Han, H. Park, S.-U. Lee, J.-H. Kim, S. W. Jeon, M. Wang, R. Avila, Z. Xi, K. Ko, M. Park, J. Lee, M. Choi, J.-S. Lee, W. G. Min, B.-J. Lee, S. Lee, J. Choi, J. Gu, J. Park, M. S. Kim, J. Ahn, O. Gul, C. Han, G. Lee, S. Kim, K. Kim, J. Kim, C.-M. Kang, J. Koo, et al., *npj Flexible Electron.* **2023**, *7*, 8.
[25] H. Han, Y. S. Oh, S. Cho, H. Park, S. Lee, K. Ko, J. Park, J. Choi, J. Ha, C. Han, Z. Zhao, Z. Liu, Z. Xie, J. Lee, W. G. Min, B. Lee, J. Koo, D. Y. Choi, M. Je, J. Sun, I. Park, *Small* **2023**, *19*, 2205048.
[26] Y. Wang, H. Wu, L. Xu, H. Zhang, Y. Yang, Z. L. Wang, *Sci. Adv.* **2020**, *6*, eabb9083.
[27] F. Zhang, Y. Zang, D. Huang, C. Di, D. Zhu, *Nat. Commun.* **2015**, *6*, 8356.
[28] Y. Yin, Y. Wang, H. Li, J. Xu, C. Zhang, X. Li, J. Cao, H. Feng, G. Zhu, *Chem. Eng. J.* **2022**, *430*, 133158.
[29] F.-L. Gao, P. Min, X.-Z. Gao, C. Li, T. Zhang, Z.-Z. Yu, X. Li, *J. Mater. Chem. A* **2022**, *10*, 18256.
[30] X.-Z. Gao, F.-L. Gao, J. Liu, Y. Li, P. Wan, Z.-Z. Yu, X. Li, *ACS Appl. Mater. Interfaces* **2022**, *14*, 43783.
[31] D. Kong, G. Yang, G. Pang, Z. Ye, H. Lv, Z. Yu, F. Wang, X. V. Wang, K. Xu, H. Yang, *Adv. Intell. Syst.* **2022**, *4*, 2200050.
[32] R. Groh, Z. Lei, L. Martignetti, N. Y. K. Li-Jessen, A. M. Kist, *Adv. Intell. Syst.* **2022**, *4*, 2100284.
[33] S. Shin, B. Ko, H. So, *Int. J. Heat Mass Transfer* **2022**, *183*, 122236.
[34] C. Pan, K. Peng, T. Chen, G. Chen, Y. Lin, Q. Zhang, M. Liu, D. Lin, T. Wang, S. Feng, *Adv. Intell. Syst.* **2023**, *5*, 2300006.
[35] C. So, Y.-S. Kim, J. H. Park, G.-Y. Kim, D. Cha, J. H. Ko, B. Kang, *Adv. Intell. Syst.* **2023**, *5*, 2200399.
[36] Z. Wan, Z. Chang, Y. Xu, Y. Huang, B. Šavija, *Adv. Intell. Syst.* **2023**, *5*, 2200333.
[37] G. Shan, X. Li, W. Huang, *Innovation* **2020**, *1*, 100031.
[38] Y. Ding, J. Yang, C. R. Tolle, Z. Zhu, *ACS Appl. Mater. Interfaces* **2018**, *10*, 16077.
[39] L. Deng, Y. Zhang, S. Wei, H. Lv, G. Chen, *J. Mater. Chem. A* **2021**, *9*, 8317.
[40] S. K. Dey, A. Hossain, M. M. Rahman, in *2018 21st Int. Conf. Comput. Inf. Technol.*, IEEE, Piscataway, NJ **2018**, pp. 1–5.
[41] D. Stursa, P. Dolezel, in *2019 22nd Int. Conf. Process Control*, IEEE, Piscataway, NJ **2019**, pp. 146–151.
[42] H. Chen, C. Zhang, H. Yu, Z. Wang, I. Duncan, X. Zhou, X. Liu, Y. Wang, S. Yang, *Appl. Energy* **2022**, *320*, 119286.
[43] J. Lv, Y. Wang, P. Ni, P. Lin, H. Hou, J. Ding, Y. Chang, J. Hu, S. Wang, Z. Bao, *Genomics* **2022**, *114*, 110426.
[44] Y. Li, W. Ma, C. Chen, M. Zhang, Y. Liu, S. Ma, Y. Yang, *IEEE Trans. Knowl. Data Eng.* **2022**, *35*, 6595.
[45] B. Ait Skourt, A. El Hassani, A. Majda, *J. King Saud Univ. Comput. Inf. Sci.* **2022**, *34*, 4756.
[46] T. Liu, H. Zhang, H. Long, J. Shi, Y. Yao, *Sci. Rep.* **2022**, *12*, 13996.
[47] A. S. Musallam, A. S. Sherif, M. K. Hussein, *IEEE Access* **2022**, *10*, 2775.
[48] R. Butola, Y. Li, S. R. Kola, C. Akbar, M.-H. Chuang, *Comput. Electr. Eng.* **2023**, *105*, 108554.
[49] C. Liu, D. Li, L. Wang, L. Li, K. Wang, *APL Mater.* **2022**, *10*, 061106.